Tensile properties and strain-hardening behavior of double-sided arc welded and friction stir welded AZ31B magnesium alloy

S.M. Chowdhury[a], D.L. Chen[a],*, S.D. Bhole[a], X. Cao[b], E. Powidajko[c], D.C. Weckman[c], Y. Zhou[c]

[a] Department of Mechanical and Industrial Engineering, Ryerson University, 350 Victoria Street, Toronto, Ontario M5B 2K3, Canada
[b] Aerospace Manufacturing Technology Centre, Institute for Aerospace Research, National Research Council Canada, 5145 Decelles Avenue, Montreal, Quebec H3T 2B2, Canada
[c] Department of Mechanical and Mechatronics Engineering, University of Waterloo, 200 University Avenue West, Waterloo, Ontario N2L 3G1, Canada

ARTICLE INFO

ABSTRACT

Microstructures, tensile properties and work hardening behavior of double-sided arc welded (DSAWed) and friction stir welded (FSWed) AZ31B-H24 magnesium alloy sheet were studied at different strain rates. While the yield strength was higher, both the ultimate tensile strength and ductility were lower in the FSWed samples than in the DSAWed samples due to welding defects present at the bottom surface in the FSWed samples. Strain-hardening exponents were evaluated using the Hollomon relationship, the Ludwik equation and a modified equation. After welding, the strain-hardening exponents were nearly twice that of the base metal. The DSAWed samples exhibited stronger strain-hardening capacity due to the larger grain size coupled with the divorced eutectic structure containing β-$Mg_{17}Al_{12}$ particles in the fusion zone, compared to the FSWed samples and base metal. Kocks–Mecking type plots were used to show strain-hardening stages. Stage III hardening occurred after yielding in both the base metal and the welded samples. At lower strains a higher strain-hardening rate was observed in the base metal, but it decreased rapidly with increasing net flow stress. At higher strains the strain-hardening rate of the welded samples became higher, because the recrystallized grains in the FSWed and the larger re-solidified grains coupled with β particles in the DSAWed provided more space to accommodate dislocation multiplication during plastic deformation. The strain-rate sensitivity evaluated via Lindholm's approach was observed to be higher in the base metal than in the welded samples.

© 2010 Elsevier B.V. All rights reserved.

1. Introduction

Weight reduction in ground vehicles and aircraft is one of the important measures to improve fuel economy and protect the environment [1]. Magnesium alloys, as the lightest metallic structural alloys, have been and will be increasingly used in the automotive and aerospace industries due to their low density [1], high strength-to-weight ratio [1–3], environmental friendliness, recyclability and castability [2,3]. However, effective joining techniques are required to further expand the applications of magnesium alloys. Friction stir welding (FSW), a solid-state joining technique developed by The Welding Institute of Cambridge, UK, in 1991 [4], has great potential for joining magnesium alloys, since it can significantly reduce weld defects normally associated with fusion welding processes [1,5]. FSW has also been used to refine the grain size via severe plastic deformation and recrystallization [6–9] so as to improve the workability of Mg alloys and increase the strength of welded joints. On the other hand, the weldability of magnesium alloys by some

arc welding processes such as gas tungsten arc welding (GTAW) is considered to be excellent as well [10]. In 1999, Zhang and Zhang [11] developed and patented a novel arc welding process referred to as double-sided arc welding (DSAW). The DSAW process uses one welding power supply and two torches; frequently a plasma arc welding (PAW) and GTAW torch each connected directly to one of the power supply terminals. The torches are positioned on opposite sides of a work-piece such that the welding current flows from one torch through the work-piece to the opposite torch. Zhang et al. [12–15] have examined the feasibility of using the DSAW process to make vertical-up, keyhole-mode welds in 6–12 mm thick plain carbon steel, stainless steel or aluminum alloy plates. More recently, Weckman and co-workers [16,17] have examined the feasibility of using the DSAW process for conduction-mode welding of 1.2 mm thick AA5182-O aluminum sheet for tailor welded blank applications. It was noted that the opposing welding torches and square-wave AC welding current successfully cleaned the oxide from both sides of the joint and produced visually acceptable welds at speeds up to 3.6 m/min. Through-thickness heating was more uniform with DSAW than with other single-sided welding processes allowing symmetric welds to be produced with minimal angular distortion of the sheets [16,17].

---

* Corresponding author. Tel.: +1 416 979 5000x6487; fax: +1 416 979 5265.
E-mail address: dchen@ryerson.ca (D.L. Chen).

Mechanical properties such as strength, ductility, strain-hardening behavior, strain-hardening sensitivity, etc., of all welds made in magnesium alloy parts used in structural applications must be evaluated to ensure the integrity and safety of the joint and structure. While there are numerous investigations on the properties of magnesium alloys, only a limited number of studies of the properties of welded magnesium alloy joints are reported. Quan et al. [18] studied the effects of heat input on microstructure and tensile properties of laser welded AZ31 Mg alloy. Liu and Dong [19] reported the effect of microstructural changes on the tensile properties in non-autogenous gas tungsten arc welded AZ31 magnesium alloy. Zhu et al. [20] presented the effect of welding parameters on the welding defects and change of microstructure in CO_2 and diode laser welded AZ31 magnesium alloy. Tensile testing has also been done on friction stir welded AZ31 [1,5,21–24], FSWed wrought AZ61 [25] and a fine-grained laser welded Mg alloy [26]. Some earlier results on the microstructural changes and strengths of various FSWed magnesium alloys and other alloys have also been well documented (e.g., in refs. [27–29]). Takuda et al. [30] performed tensile tests on a Mg–9Li–1Y alloy at room temperature and observed that the values of strain-hardening exponents increased with increasing strain rate. Afrin et al. [24] obtained similar results for a FSWed AZ31B-H24 Mg alloy. Yu et al. [31] evaluated the tensile strength of FSWed thixomolded AE42 Mg alloy, but no information on strain-hardening and strain-rate sensitivity was given, while Lee et al. [32] studied the formability of friction stir welded AZ31 magnesium alloy sheet and other alloys experimentally and numerically. Some authors have studied the strain-hardening behavior of magnesium alloys with emphasis on the relationships between the grain size strengthening and dislocation strain hardening of the material [2,24,33–35]. While Shen et al. [36] have evaluated the formation of macropores in double-sided gas tungsten arc welded wrought magnesium AZ91D alloy plates made with two separate passes (i.e., welded with one partial penetration weld on the top side and then a separate partial penetration weld on the back side of the plate), the mechanical properties of conduction-mode double-sided arc welds made in magnesium alloy sheet have not been examined. It is unknown if this novel arc welding technique could be used to produce welds in magnesium alloys with acceptable mechanical properties. The aim of the present investigation, therefore, was to evaluate and compare the microstructure, tensile properties, strain-hardening and strain-rate sensitivity of DSAWed and FSWed AZ31B-H24 Mg alloy sheet.

2. Materials and experimental procedure

In the present study, 2 mm thick AZ31B-H24 Mg alloy sheet was used. The nominal chemical composition of this alloy was 2.5–3.5 wt% Al, 0.7–1.3 wt% Zn, 0.2–1.0 wt% Mn and balance Mg [37]. Two different welding methods, DSAW and FSW, were employed to make autogenous welds between the work-pieces in the butt joint configuration. Both DSAWed and FSWed joints were made with the welding direction perpendicular to the rolling direction of the sheet. In the DSAW process, a PAW torch and a GTAW torch were used with a square-wave AC welding power supply. A detailed description of the welding apparatus and other process parameters used may be found in [16,17]. Prior to DSAW, the work-pieces were degreased using acetone and then alcohol. The oxide on the surface of the sheets was then mechanically removed in the area of the weld using a stainless steel wire brush. The DSAW welds were made using a welding speed of 25 mm/s and welding power of 1.4 kW. The FSW welds were made using a welding speed of 10 mm/s and a right-hand threaded pin tool having a pin length of 1.65 mm rotating clockwise at a rate of 2000 rpm. Prior to FSW, surface oxides were removed with a steel brush and then the surface was cleaned using ethanol as well.

The welded joints perpendicular to the welding direction were cut and cold mounted in order to examine the microstructure of the fusion zone (FZ), heat-affected zone (HAZ) and base metal (BM). The mounted samples were manually ground, polished, and etched using acetic picral (10 mL acetic acid (99%), 4.2 g picric acid, 10 mL H_2O, 70 mL ethanol (95%)) [38]. The microstructure was observed with an optical microscope equipped with quantitative image analysis software. Vickers microhardness tests were conducted with a computerized Buehler machine across the sectioned weld with a spacing of 0.5 mm. A load of 100 g and dwell time of 15 s were applied during the hardness tests. Sub-sized tensile specimens in accordance with ASTM E8M-08 standard [39] were machined along the rolling (or longitudinal) direction for both the base metal and welded joints, where the weld was positioned at the center of the gauge area. Tensile tests were performed using a computerized tensile testing machine at constant strain rates of 1×10^{-2}, 1×10^{-3}, 1×10^{-4} and 1×10^{-5} s^{-1} at room temperature. At least two samples were tested at each strain rate. The fracture surfaces were examined using a scanning electron microscope (SEM) equipped with an energy dispersive X-ray spectroscopy (EDS) system and 3D fractographic analysis capacity.

3. Results and discussion

3.1. Microstructure

The microstructure of the AZ31B-H24 Mg base metal is shown in Fig. 1, where elongated and pancake-shaped grains with varying sizes were observed. The heterogeneity in the grain structure of the base metal was due to both deformation of the 2 mm thick sheet by rolling and incomplete dynamic recrystallization (partial annealing) [1]. The average grain size of the base metal was about 5 μm. The typical macroscopic and microscopic structures of FSWed AZ31B-H24 Mg alloys are shown in Fig. 2. Fig. 2(a) shows the top weld bead after FSW and Fig. 2(b) presents a typical cross-section of the FSWed sample including HAZ, thermomechanically affected zone (TMAZ) and stir zone (SZ). As seen in Fig. 2(c), both equiaxed and elongated grains were present in the HAZ. However, in comparison to the base metal (Fig. 1), far more equiaxed grains appeared in the HAZ, indicating that partial recrystallization had also taken place during FSW. The recrystallization temperature of the alloy was approximately 205 °C. Thus, the temperature in part of the HAZ may have been above this value. This is confirmed by some large grains observed in the HAZ due to grain growth after recrystallization [1]. The grain structure in the TMAZ (Fig. 2(d)) in the present study is basically equiaxed and recrystallized, which
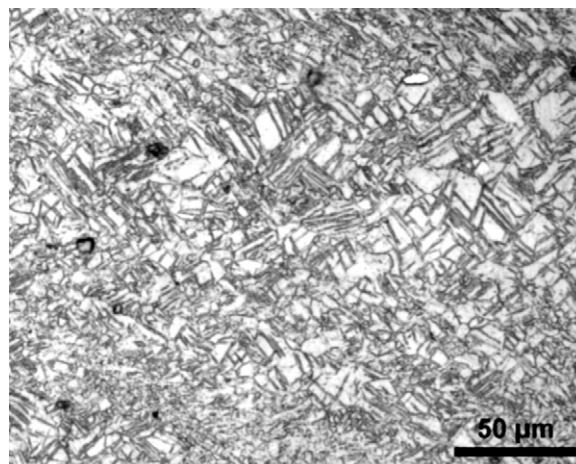

Fig. 1. Typical microstructures of the base metal (BM) of the AZ31-H24 Mg alloy.
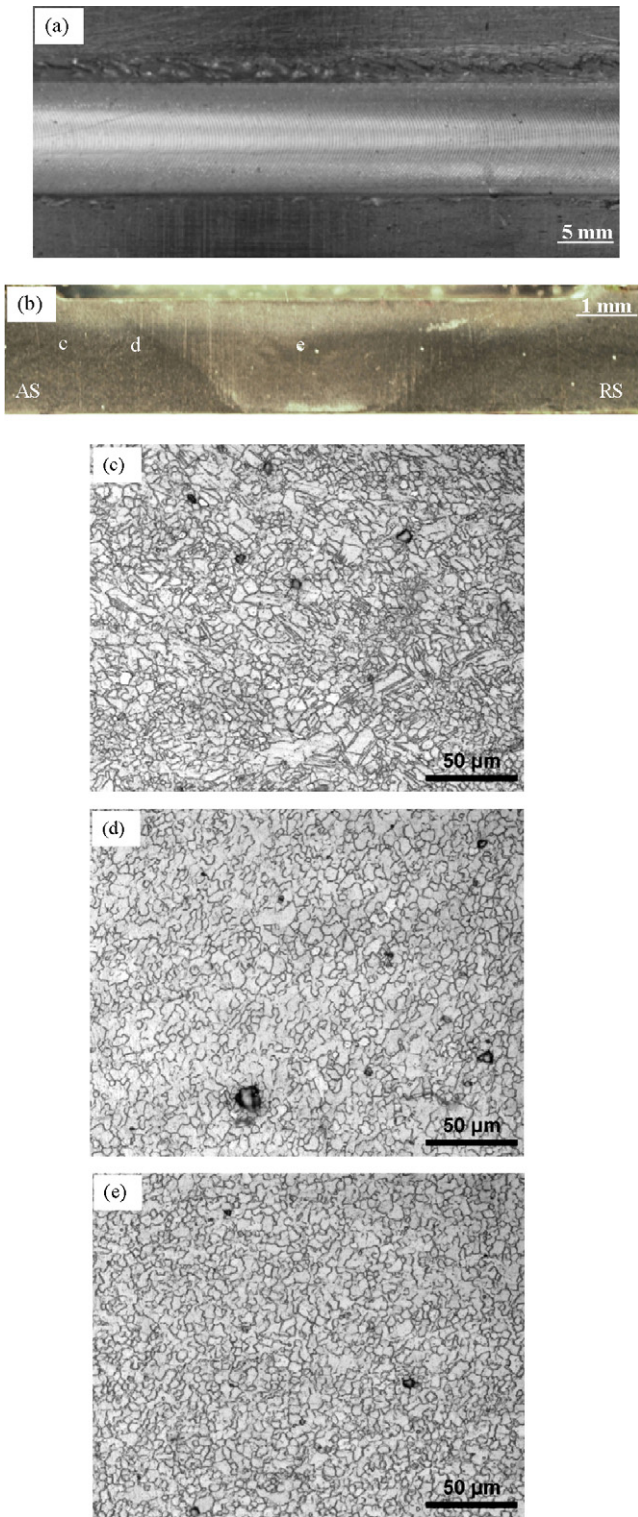
Fig. 2. Typical macroscopic and microscopic structures of a friction stir welded AZ31-H24 alloy. (a) Top weld bead surface, (b) cross-section of the welded joint, (c) heat-affected zone (HAZ), (d) thermomechanically affected zone (TMAZ), and (e) stir zone (SZ).

was similar to the recent results reported by Cao and Jahazi [1] and Afrin et al. [5,40], while it was different from earlier observations [41] where the TMAZ was still characterized by deformed and elongated grains. The grains in the SZ were equiaxed (Fig. 2(e)) and became noticeably bigger in the center of the stir zone (~8 μm). These changes were caused by dynamic recrystallization during
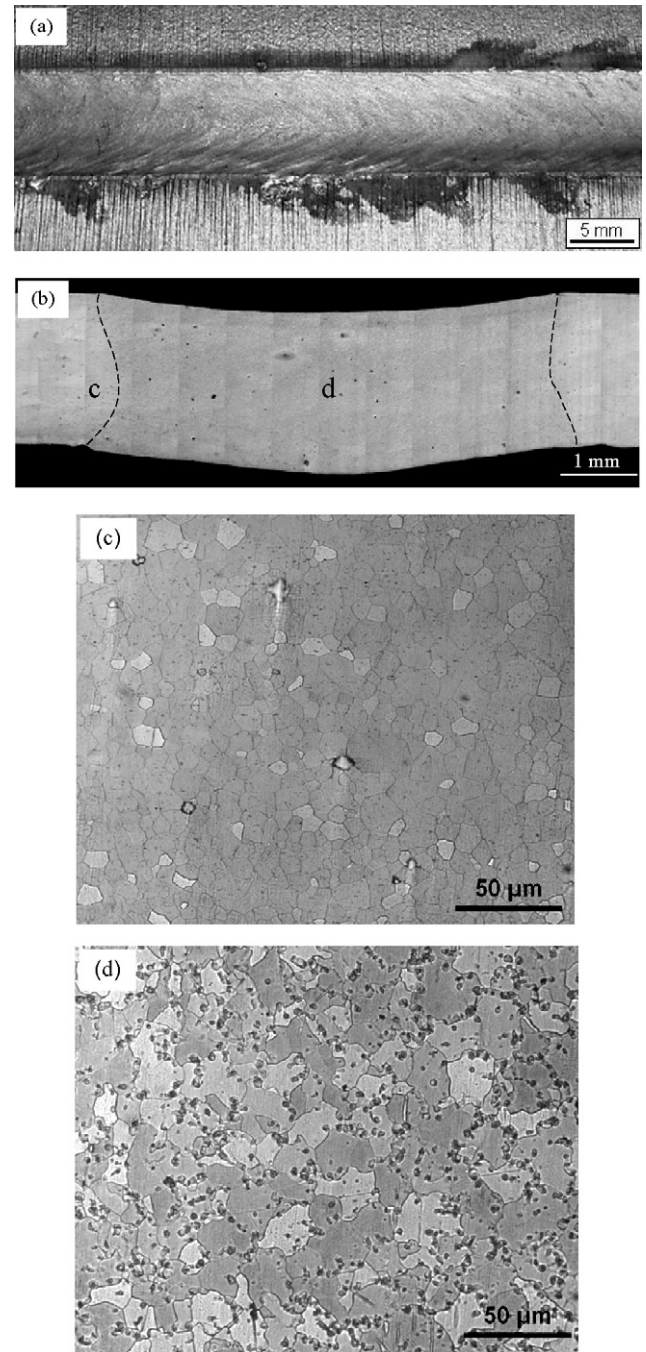

Fig. 3. Typical macroscopic and microscopic structures of a double-sided arc welded AZ31-H24 alloy. (a) Top weld bead surface, (b) cross-section of the welded joint, (c) heat-affected zone (HAZ), and (d) fusion zone (FZ).

FSW [42]. A larger grain size in the SZ was also reported by Cao and Jahazi [1], Afrin et al. [5], Fairman et al. [40], Pareek et al. [43], and Lim et al. [44].

Fig. 3(a) and (b) shows the top weld bead surface and a cross-section of the DSAW weld, respectively. It is seen that the top weld bead quality appeared excellent with complete cleaning of the oxide. The bottom weld bead surface was similar to the top. As shown in Fig. 3(b), there was a slight sagging of the weld pool due to the effects of gravity on the molten pool during welding. Fig. 3(c) shows an equiaxed microstructure of the HAZ in the DSAWed sample that was completely recrystallized. The grain size in the HAZ of DSAWed sample (Fig. 3(c)) was larger than that in the HAZ of
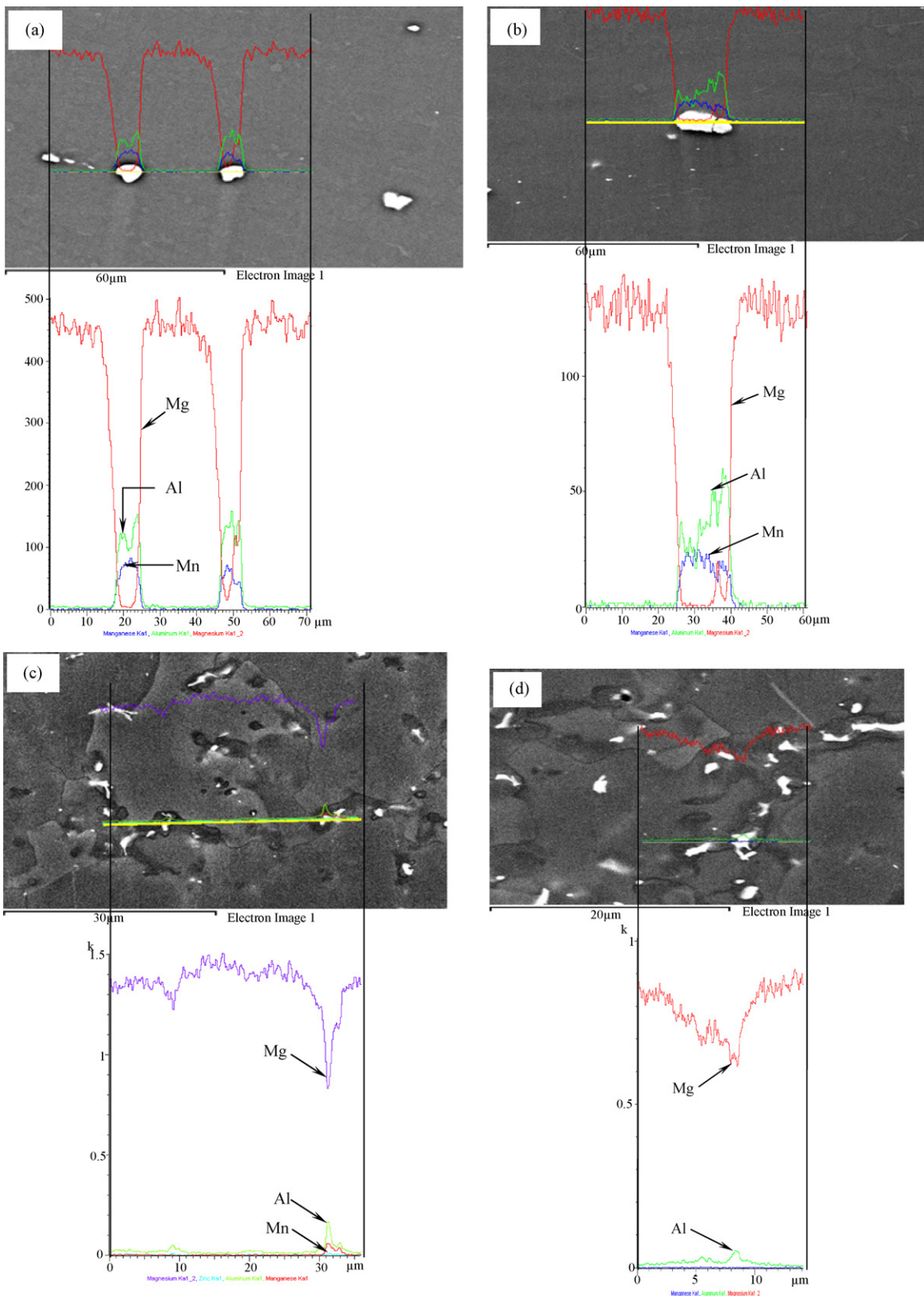
Fig. 4. EDS line scan showing the compositional variation across the particles in (a) base metal, (b) heat-affected zone (HAZ), (c) and (d) fusion zone (FZ) of a DSAWed joint.

the FSWed sample (Fig. 2(c)). This was attributed to the higher temperature experienced in the HAZ of the DSAWed sample. The fusion boundary had a slight hour glass shape (Fig. 3(b)) and the grain size in the FZ (Fig. 3(d)) became further larger (~15 μm) with β (Mg$_{17}$Al$_{12}$) phase particles arising from a divorced eutec-

tic that formed in the interdendritic and intergranular regions of the solidification microstructure in the FZ.

EDS analysis indicated that some Mn–Al containing parti-cles/inclusions were present in the base material, as shown in Fig. 4(a). Similar results were observed by Lin and Chen [45].
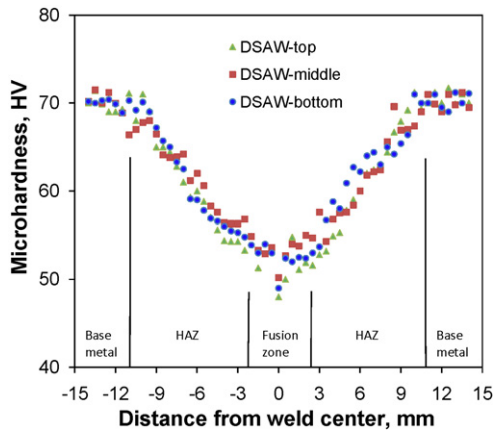
Fig. 5. Microhardness profile across a DSAWed sample.

Fig. 6. Typical engineering stress versus engineering strain curves of the AZ31B-H24 base alloy, FSWed and DSAWed samples tested at a strain rate of 1×10^{-5} s^{-1}.

Fig. 4(b) shows a typical particle in the heat-affected zone. Line scan with EDS analysis signified that these particles were similar to those Mn–Al containing particle observed in the base metal (Fig. 4(a)), in spite of the remainder of the material experiencing a transition of microstructure in the HAZ (Fig. 3(c)). Fig. 4(c) revealed clearly a divorced eutectic structure in the FZ of the DSAWed sample, with both β phase particles on the left-hand side and the unmelted Mn–Al containing particle on the right-hand side along the grain boundary, although both particles had the same white color on the image. The eutectic-like structure consisting of alternating eutectic α-Mg and eutectic β-Mg$_{17}$Al$_{12}$ along the grain boundary could be seen in Fig. 4(d). The presence of the eutectic-like structure was due to the fast non-equilibrium cooling of the weld pool after welding, since no normal eutectic structure in the form of alternating layers of α and β would be possible in the AZ31 Mg alloy containing only 3 wt% Al based on the equilibrium phase diagram if the cooling rate would be infinitely slow (i.e., under equilibrium cooling). As seen in Fig. 4(c) and (d) and Fig. 3(d) there were also many β-Mg$_{17}$Al$_{12}$ particles within the grains. Liu et al. [46] studied laser/arc hybrid welding behavior on Mg alloy and reported that many "spot" precipitates formed within the Mg grain were likely to be the β-Mg$_{17}$Al$_{12}$ phase. Liu et al. [47] also observed Mg–Al intermetallic brittle phase in the FZ of TIG welded Mg/Al dissimilar joints. Ben-Hamu et al. [48] studied GTA welded AZ31B Mg alloy and reported that the fusion zone microstructure consisted of a cored α-Mg matrix and a divorced eutectic in the interdendritic regions which were originally Mg$_{17}$Al$_{12}$ that subsequently transformed to τ phase (Mg$_{32}$(Al,Zn)$_{49}$) intermetallics. Electron beam welding and gas tungsten arc welding had been employed to weld AZ91 and AZ31B Mg alloys, respectively, by Su et al. [49] and Padmanaban et al. [50], and they observed fine equiaxed grains with intergranular β-Mg$_{17}$Al$_{12}$ precipitates as well.

3.2. Microhardness

A typical hardness profile across the DSAWed AZ31B-H24 Mg alloy is shown in Fig. 5. It is seen that the hardness value decreased gradually from about HV 70 in the half-hardened H24 temper BM to approximately HV 50 at the center of the FZ of the welded joints. This is due to the formation of non-equilibrium cast structures in the FZ (Fig. 3(d)), in conjunction with a larger grain size in the FZ in comparison with that in the HAZ (Fig. 3(c)) and in the BM (Fig. 1). Furthermore, the grain shape had a significant change from the deformed and elongated (or pancake-shaped) grains in the half-hardened H24 condition (Fig. 1) to the fully annealed or recrystallized equiaxed grains in the HAZ (Fig. 3(c)). All of these factors led to the hardness change shown in Fig. 5. Similar results
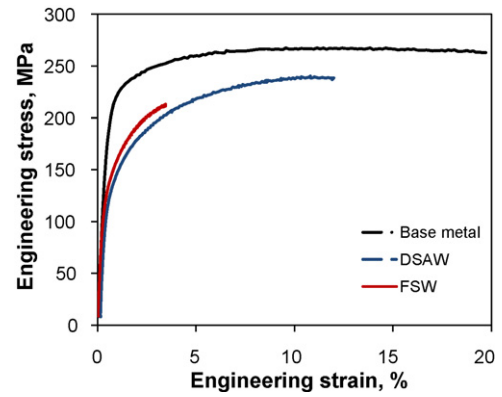
were observed for the FSWed joints, where the lowest hardness occurred at the center of stir zone as well.

3.3. Tensile properties

Fig. 6 shows typical engineering stress versus engineering strain curves of the base metal, FSWed and DSAWed AZ31 Mg alloy sheets tested at a strain rate of 1×10^{-5} s^{-1}. It is seen that after welding, both the strength and elongation were reduced. While the FSWed sample had higher yield strength (YS), the DSAWed sample had a higher ultimate tensile strength (UTS) and elongation. A joint efficiency of about 83% was achieved for the DSAWed joints, but it was only about 72% for the FSWed joint. Fig. 7 presents the effect of strain rate on the tensile properties. It was clear that the YS and UTS increased and ductility (%El) decreased with increasing strain rate for the base metal, but the effect of strain rate on the YS, UTS and %El became smaller after both types of welding. Similar effect of strain rate on the YS and UTS was also reported in Mg–9Li–1Y [30], AM30 [51], cryo-rolled Cu [52] and AZ31B alloys [2,24,53].

Both the UTS and %El of the DSAWed joints lay in-between those of the base metal and the FSWed joints. The reason behind this was the presence of a significant welding defect observed near the bottom surface of FSWed samples using a right-hand threaded pin tool, as shown in Fig. 8. The welding defect could be better seen from the SEM images taken from a fracture surface after tensile testing at a strain rate of 1×10^{-3} s^{-1} shown in Fig. 9(a) at a lower magnification and Fig. 9(b) at a higher magnification. Similar defects were also observed by Cao and Jahazi [1] who noted that the upward movement of the material in the stir zone may cause the formation of subsurface porosity or even root notches near the bottom surface of the work-piece when the right-hand pin was used. It is clear that such defects at the bottom surface in the FSWed joints would lead to a strong notch effect or stress concentration and have a significant influence on the mechanical properties, causing premature failure as shown in Fig. 6. As a consequence, both the UTS and ductility of the FSWed samples were reduced notably (Fig. 7(b) and (c)), in spite of the slightly higher YS (Fig. 7(a)), in comparison with those of DSAWed joints.

It has recently been reported that tool profiles and axial force (downward force) have a significant effect on the defect-free FSWed joint in an Al alloy and the subsequent tensile properties [54]. To understand the effect of axial force and tool pin profile, five different tool pin profiles and three different axial force levels to the butt joint of Al6061 Al alloy were examined. Square pin profiled tools were observed to produce defect-free, good quality friction stir regions, regardless of the applied axial force levels. On the other hand, additional axial force (7 kN) increased heat input and led to defect-free, good quality friction stir regions as well, irrespective of
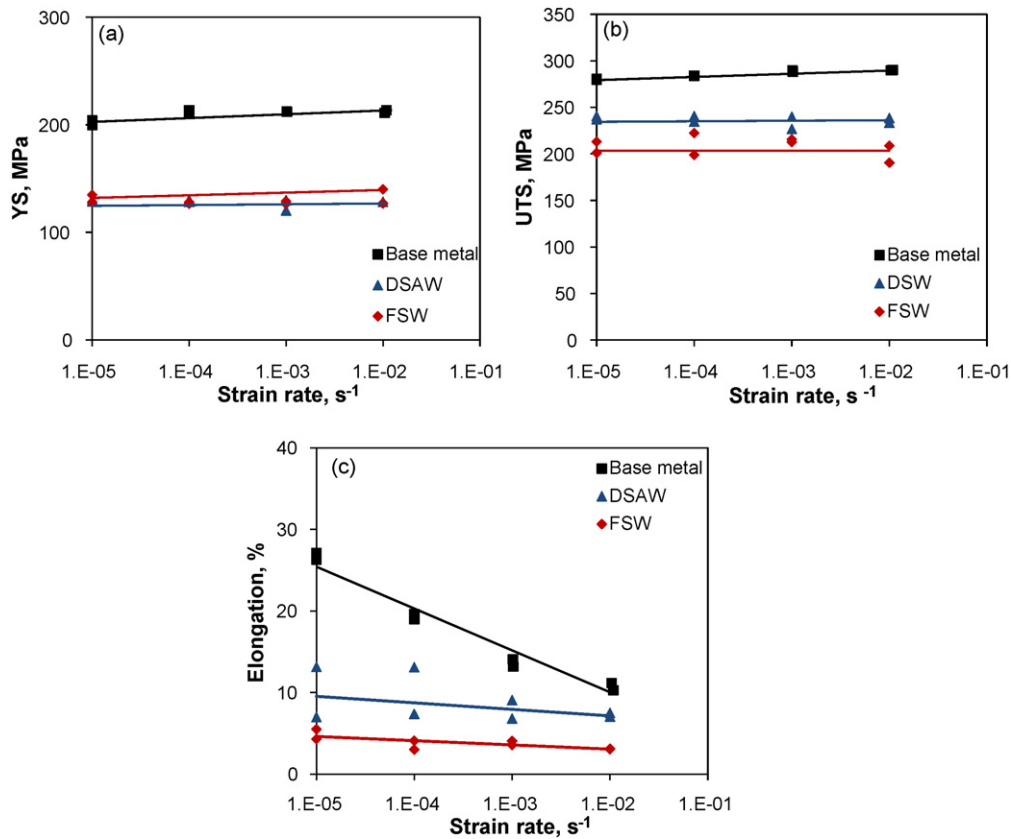
Fig. 7. Effect of strain rate on (a) yield strength (YS), (b) ultimate tensile strength (UTS), and (c) ductility of the base metal, FSWed and DSAWed samples.

tool pin profiles [54]. In the present study, a cylindrical tool with right-handed threads was used for the FSWed joints. During FSW operation it was observed that metal flowed up and stuck to the pin ends due to the use of right-handed threads in the rotating tool. The subsurface porosity and notch defect at the bottom surface were not observed in the FSW when using left-handed pin tools in the same clockwise rotation [5]. This suggests that the observed welding defects at the bottom surface of FSWed joints as shown in Figs. 8 and 9 were due to the use of a right-hand threaded pin tool rotated clockwise.
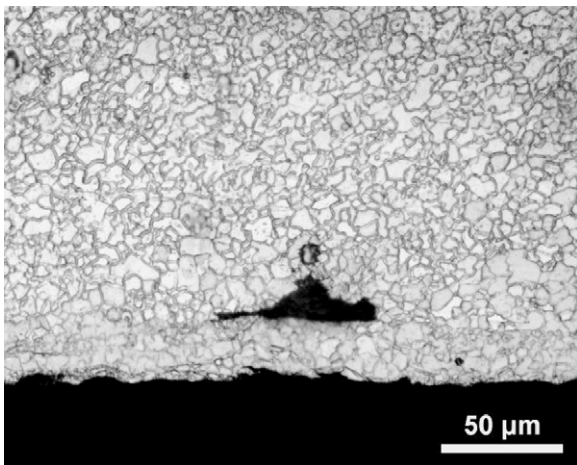

Fig. 8. An OM micrograph of a FSWed sample near the bottom surface at a welding speed of 10 mm/s and rotational rate of 2000 rpm using a right-hand threaded pin in the clockwise rotation.

The tensile test data are summarized in Fig. 10, where the strength was presented as a function of the ratio of the welding speed (v) to the rotational rate (ω). Despite the presence of the welding defects at the bottom surface of the FSWed joints, the UTS was still equivalent to those reported in the literature at various welding speeds and tool rotational rates [5,43,44]. The YS obtained in the present study was indeed higher than those reported in the literature [5,43,44]. The fact that the pores did not have a strong effect on the YS but the UTS could be reduced was simply due to the reduced ductility. That is, the sample failed due to strain localization around the defects before the UTS was reached. The number of these defects appeared to have a dominant effect on the true strain of the welded joint at localization. These voids, which were internal to the material, resulted in a reduced cross-sectional area in the gauge area of the material [55]. Some authors also observed significant interactions between the surface defect and pores that enhanced the formation of macroscopic shear bands, which promoted the failure [56]. Therefore, to increase the UTS and ductility it is necessary to minimize or avoid the weld defects during FSW.

3.4. Strain-hardening behavior

The hardening capacity of a material may be considered as a ratio of the ultimate tensile strength σ_{UTS}, to the yield strength σ_y [24,57]. Afrin et al. [24] re-defined a normalized parameter of hardening capacity, H_c, as follows:

$$H_c = \frac{\sigma_{UTS} - \sigma_y}{\sigma_y} = \frac{\sigma_{UTS}}{\sigma_y} - 1 \tag{1}$$

The obtained hardening capacity of the base metal and the welded samples is listed in Table 1. It is seen that the hardening capacity was enhanced after FSW, similar to the results reported
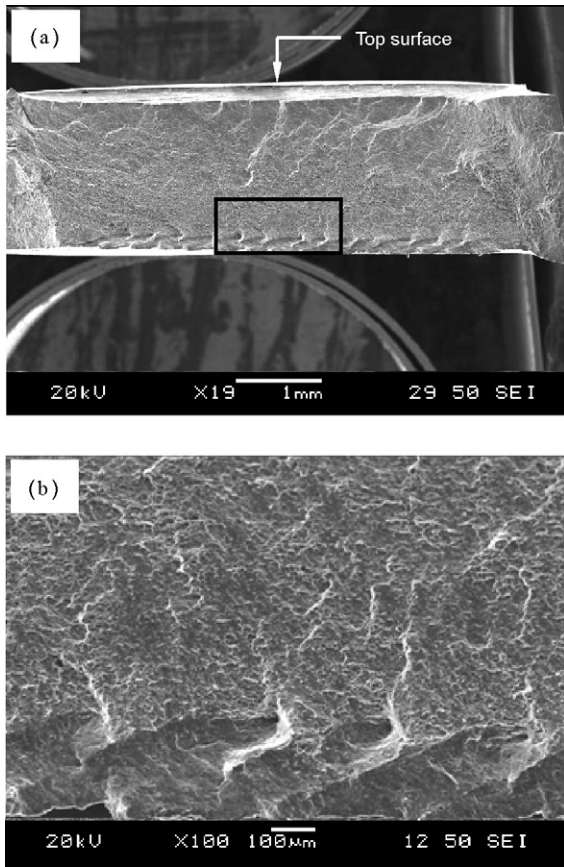
Fig. 9. SEM images of fracture surfaces of a FSWed sample tested at a strain rate of 1×10^{-3} s^{-1}. (a) Overall view at a lower magnification, and (b) details of welding defects at a higher magnification.

by Afrin et al. [24]. The hardening capacity in the DSAWed samples was further higher than that in the FSWed samples. There was little effect of the strain rate on the hardening capacity. Based on Eq. (1) the hardening capacity of a material was related to its yield strength that was further associated with the microstructure and texture of the material. An increase in the grain size would decrease the YS according to the Hall–Petch relationship [58–60] and increase dislocation storage capacity, leading to the higher hardening capacity. A decrease in the grain size reduced the difference of the flow resistance between the grain boundary and interior, which in turn
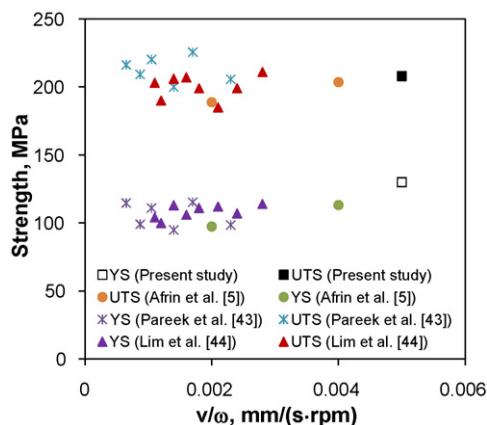

Fig. 10. A comparison of the YS and UTS, as a function of the ratio of the welding speed (v) to the rotational rate (ω), obtained in the present study with those reported in the literature.

Table 1
Hardening capacity of the base alloy, FSWed and DSAWed samples tested at different strain rates.

Specimen	Strain rate (s^{-1})	Hardening capacity
Base metal	1×10^{-2}	0.37
	1×10^{-3}	0.36
	1×10^{-4}	0.36
	1×10^{-5}	0.41
Friction stir welded sample	1×10^{-2}	0.49
	1×10^{-3}	0.67
	1×10^{-4}	0.66
	1×10^{-5}	0.57
Double-sided arc welded sample	1×10^{-2}	0.84
	1×10^{-3}	0.86
	1×10^{-4}	0.84
	1×10^{-5}	0.84

reduced the hardening capacity [57]. Since the grain size of the DSAWed samples was larger than that of FSWed sample, as shown in Figs. 3(d) and 2(e), respectively, the higher value of hardening capacity in the DSAWed samples would be anticipated. In addition, it should be noted that for rolled Mg plates there was usually a strong texture with the (0 0 0 2) plane perpendicular to the transverse direction (TD) and normal direction (ND) of the plate [61]. However, after FSW and DSAW the texture would be expected to be weakened. Yang et al. [61] reported that after FSW a significant change of texture was observed with a high intensity of (0 0 0 2) diffraction around the TMAZ, and the FSWed joint prone to slip along the (0 0 0 2) with an orientation of ~45° at a lower critical resolved shear stress exhibited an approximately one third drop in the yield strength but only a modest decrease in the ultimate tensile strength. This implied that the hardening capacity after FSW increased as well, in good agreement with the results observed in the present study.

To understand strain-hardening behavior it is better to examine the strain-hardening exponent of different materials. The strain-hardening exponent is a measure of the ability of a metal to strain harden; the larger its magnitude, the greater the strain hardening for a given amount of plastic strain [58]. Several researchers have proposed different equations to evaluate the strain-hardening exponent. Hollomon [62] gave the following expression:

$$\sigma = K\varepsilon^n, \tag{2}$$

where n is the strain (or work) hardening exponent, K is the strength coefficient, σ is the true stress and ε is the true strain [60,62–64]. To better quantify the strain-hardening response, Chen and Lu [65] fitted their tensile curves using the Ludwik equation [64,66]:

$$\sigma = \sigma_y + K_1\varepsilon^{n1} \tag{3}$$

where n_1 is the strain-hardening exponent and K_1 is the strength coefficient which represents the increment in strength due to strain hardening at $\varepsilon = 1$. Afrin et al. [24] proposed the following equation using net flow stress and net plastic strain of materials after yielding:

$$\sigma = \sigma_y + K^*(\varepsilon - \varepsilon_y)^{n^*} \tag{4}$$

where n^*, σ, ε, σ_y and ε_y are the strain-hardening exponent, true stress, true strain, yield strength and yield strain of a material, respectively. K^* is the strength coefficient which reflects the increment in strength due to strain hardening corresponding to $(\varepsilon - \varepsilon_y) = 1$. The above three equations could be better illustrated in Fig. 11. Eq. (2) has the origin positioned at O (including the elastic deformation stage where the Hooke's law holds true), although only the data in the uniform deformation stage between the YS and UTS are used. Eq. (3) corresponds to a shift of the origin from O to O_1 in Fig. 11 where the yield stress is excluded, while Eq. (4) proposed
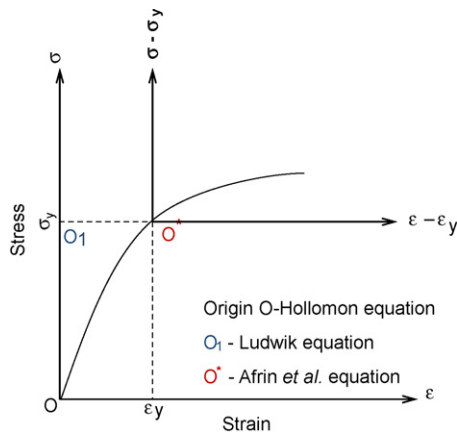
Fig. 11. Schematic illustration of a true stress versus true strain curve.

recently by Afrin et al. [24] represents a further shift of the origin from O_1 to O^*. It implies that both the yield stress and yield strain are precluded. Fig. 12 presents the evaluated strain-hardening exponents (n, n_1, n^*) as a function of strain rate for the base metal, FSWed and DSAWed samples. Almost no effect of strain rate on the strain-hardening exponents was seen in the base metal. But for the DSAWed and FSWed samples, the strain-hardening exponents increased with increasing strain rate. The strain-hardening exponents evaluated according to all the above three equations were obviously higher after welding, and the DSAW resulted in somewhat higher strain-hardening exponents than the FSW, as shown in Fig. 12. It is also seen that the n values were the smallest and n_1 values were the highest with n^* lying in-between the two. Similar results were also reported by Afrin et al. [24].
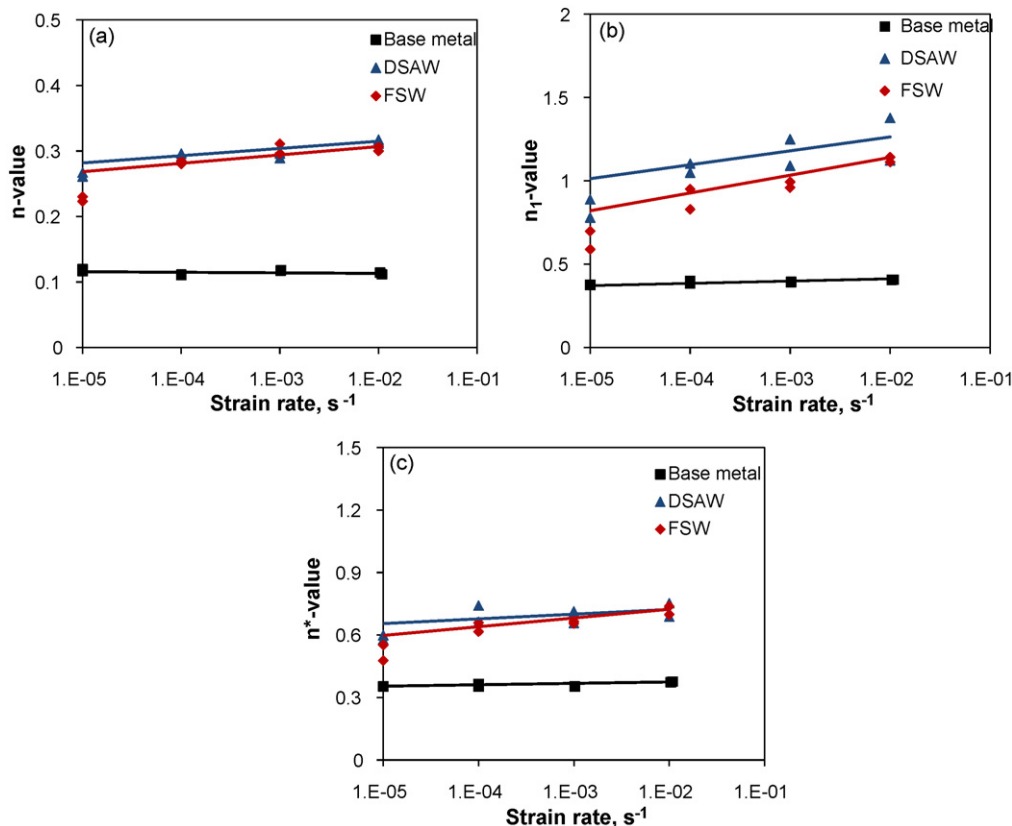
One of the most important contributions to the strain hardening is related to the formation and multiplication of dislocations. In the plastic deformation stage, the net flow stress due to dislocation density could be expressed as [24,33,34]:

$$\sigma - \sigma_y \propto \sqrt{\rho} \tag{5}$$

where ρ is the dislocation density. The net flow stress necessary to continue deformation of a material is proportional to the square root of the dislocation density. The dislocation density in a metal increases with deformation or cold work due to dislocation multiplication or the formation of new dislocations which decreases the spacing among dislocations and their interactions become repulsive. The net result would be that the motion of a dislocation is impeded by other dislocations. As the dislocation density increases, the resistance to dislocation motion by other dislocations becomes more pronounced. Thus, a higher stress is necessary to deform a metal [58].

Fig. 13 shows a typical Kocks–Mecking plot of strain-hardening rate ($\theta = d\sigma/d\varepsilon$) versus net flow stress ($\sigma - \sigma_y$) at different strain rates from $1 \times 10^{-2}\,\text{s}^{-1}$ to $1 \times 10^{-4}\,\text{s}^{-1}$ for the base metal. It is seen that no stage I hardening (or 'easy glide') which depends strongly on the orientation of the crystal and stage II linear hardening where the strain-hardening rate should be constant occurred. Srinivasan and Stoebe [67] reported that the presence of stage II strain hardening could be due to the interactions of the dislocations in the primary slip system with those in an intersecting slip system. Stage III hardening is characterized by a hardening rate that decreases monotonically with increasing flow stress leading to the much repeated term "parabolic hardening" on the stress strain curve [68]. This stage is very sensitive to the temperature and rate of deformation [33]. In this present study test temperature remained constant but strain rates were changed. As seen from Fig. 13, stage III was somewhat strain-rate sensitive, i.e., the

Fig. 12. Effect of strain rate on (a) n-value, (b) n_1-value and (c) n^*-value in the base metal, FSWed and DSAWed samples.
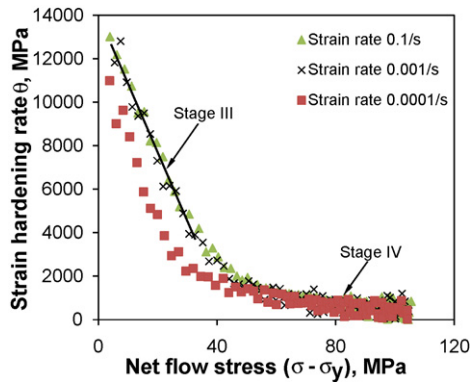
Fig. 13. strain-hardening rate (θ) versus net flow stress ($\sigma - \sigma_y$) of the base metal tested at different strain rates.

strain-hardening rate increased with increasing strain rate. Similar result was observed by Lin and Chen [2] in AZ31B extruded Mg alloy as well. This could be explained on the basis of the following equation [2,33]:

$$\theta = \theta_0 - \frac{R_d \sigma}{\dot{\varepsilon}^{1/q}} \tag{6}$$

where θ is the strain-hardening rate in stage III, θ_0 is a constant, q is an experimental stress exponent varying with temperatures and is rather large namely about $n = 8$ at higher and $n = 35$ at lower temperatures, R_d is also a temperature dependent parameter. In the present experiments R_d and q were constant as temperature remained constant. It is evident from Eq. (6) that the strain-hardening rate increased with increasing strain rate at a given stress.

As stage III approached a saturation level, hardening stage IV appeared. Due to the low hardening level of stage IV, it is difficult to track the hardening mechanisms because they must compete with geometrical and structural instabilities including damage [33]. However, Pantleon [69] reported that stage III hardening was extended to stage IV by incorporation of excess dislocations related to the disorientations. He further stated that in stage IV the work hardening rate often remains constant. It is seen from Fig. 14 that stage IV in the base metal remained almost constant with a low strain-hardening rate.

Fig. 14 shows a typical Kocks–Mecking plot of strain-hardening rate versus net flow stress in the base metal, FSWed and DSAWed samples tested at a strain rate of $1 \times 10^{-2}\,\mathrm{s^{-1}}$. At lower strains or net flow stress levels after yielding the strain-hardening rate of the base metal was higher than that of the welded joints. At higher strains or net flow stress levels it was reversed. The strain hardening could be understood on the basis of the grain size strengthening and
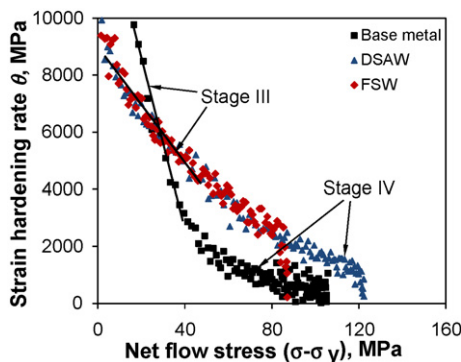
dislocation strain hardening [24,34,35]:

$$\sigma = \sigma_0 + \sigma_{HP} + \sigma_d, \tag{7}$$

where σ_0 is the frictional contribution, $\sigma_{HP} = kd^{-1/2}$ is the Hall–Petch contribution and $\sigma_d = M\alpha Gb\rho^{1/2}$ is the Taylor dislocation contribution (where G is the shear modulus, b is the Burgers vector, M is the Taylor factor and α is constant). Sinclair et al. [70] and Kovacs et al. [71] reported that at lower strains the grain size had a strong contribution to the strain hardening and the influence of the grain size on the strain hardening vanished at higher strains due to dislocation screening and dynamic recovery effects at grain boundaries. Since the base metal had a smaller grain size coupled with its deformed grain structure, the Hall–Petch contribution (σ_{HP}) would be stronger at lower strains, leading to a higher strain-hardening rate in comparison with the welded joints. On the other hand, at higher strains or later stage of deformation strain hardening was higher in the welded joints. This could be due to the larger grain size and the presence of β particles in the fusion zone of the DSAWed samples. It was stated that the presence of precipitates increased the dislocation density [72] and larger grain size provided more space to accommodate dislocations [24]. As the grain size of the DSAWed samples was larger, a strong strain-hardening rate was observed after DSAW in comparison with the FSW and the base metal (Fig. 14). This is also in agreement with other observations where the hardening rate decreasing with decreasing grain sizes in AZ31 alloy was presented [24,34,73]. However, due to the presence of weld defects at the bottom surface, the FSWed samples failed prematurely, thus the net flow stress up to failure in the FSWed sample was the lowest (Fig. 14).

Another important parameter involving the deformation behavior of materials was the strain-rate sensitivity (SRS), m. The Lindholm [74] approach was used to evaluate the SRS based on the following equation:

$$\sigma = \sigma_0(\varepsilon) + \sigma_1(\varepsilon) \log \dot{\varepsilon} \tag{8}$$

The Lindholm SRS is $\sigma_1(\varepsilon)$ in the equation commonly termed as m_L. The plot of σ versus $\log \dot{\varepsilon}$ at 2.5% true strain is shown in Fig. 15, where Lindholm SRS is represented by the slope, m_L. The m_L values for the base metal, DSAWed joins and FSWed joints were 7, 4 and 3.5, respectively. It follows that the SRS became lower after welding, which would be related to the difference in the microstructure and flow stress. del Valle and Ruano [35] have recently presented a relationship between stress, SRS and grain size for the AZ31 alloy as follows:

$$\frac{\partial \sigma}{\partial \ln \dot{\varepsilon}} = \frac{k}{2} d^{-1/2}(M_c - 2M_{cg}) + \sigma M_{cg}, \tag{9}$$

Fig. 14. strain-hardening rate (θ) versus net flow stress ($\sigma - \sigma_y$) of the base metal, FSWed and DSAWed samples tested at a strain rate of $1 \times 10^{-2}\,\mathrm{s^{-1}}$.
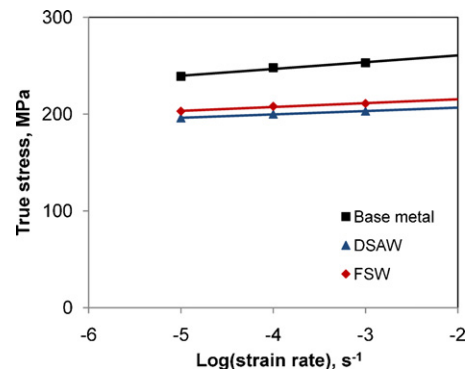

Fig. 15. A typical plot used to evaluate the strain-rate sensitivity, m_L, at a true strain value of 2.5% via the Lindholm's approach for the base metal, DSAWed and FSWed samples.
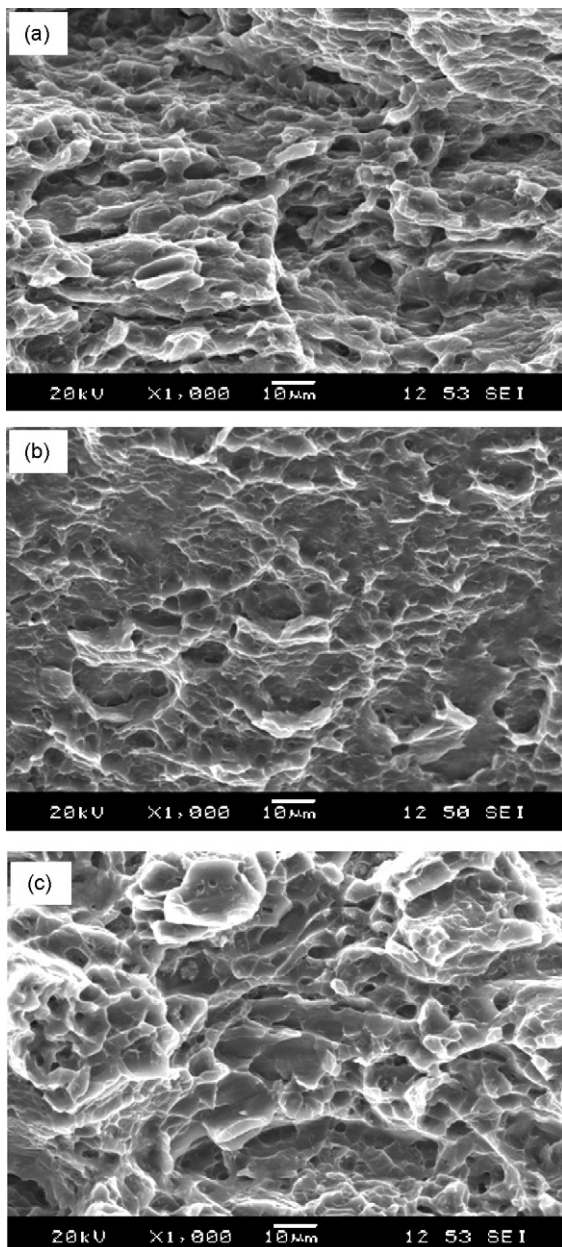
Fig. 16. Typical SEM images showing the fracture surfaces of samples tested at a strain rate of $1 \times 10^{-3}\,\mathrm{s}^{-1}$. (a) Base metal, (b) FSWed sample, and (c) DSAWed sample.

where k is Boltzmann constant, d is the grain size, σ is the flow stress, $M_{cg} = \partial \ln \sigma_{cg}/\partial \ln \dot{\varepsilon}$ and $M_c = \partial \ln \tau_c/\partial \ln \dot{\varepsilon}$. This equation represents a linear correlation between the SRS, flow stress σ and grain size in the form of $d^{-1/2}$. It means that the SRS increased with decreasing grain size. Since the base metal had a smaller grain size and higher flow stress, its SRS would be higher in comparison with that of the welded joints. This is in agreement with the results reported by del Valle and Ruano [35] and Prasad and Armstrong [75].

3.5. Fractography

Fig. 16 shows typical images of the fracture surfaces of the base metal, FSWed and DSAWed samples tested at a strain rate of $1 \times 10^{-3}\,\mathrm{s}^{-1}$. It is seen from Fig. 16(a) that dimple-like elongated fracture appeared more apparent. This type of fracture surface denoted ductile fracture that was characterized by cup-like depres-

sions [59]. Some inclusions were present on the fracture surface of AZ31B rolled magnesium alloy. Similar fracture surface characteristics were reported in [2,5]. As shown in Fig. 16(b), some cleavage-like flat facets in conjunction with dimples and river marking could be seen in the FSWed sample. The river marking was caused by the crack moving through the grain along a number of crystallographic planes which formed a series of plateaus and connecting ledges [59]. The fractographic observations corresponded well to the relatively low percentage elongation of ~4% in the FSWed samples. While tensile fracture initiation could have started from the area between the weld nugget and the TMAZ as reported by Lim et al. [44], the crack initiation occurred from the welding defect at the bottom surface in the present study (Figs. 8 and 9). In the DSAWed sample, more dimples together with fewer cleavage-like facets were observed, as shown in Fig. 16(c). The crack initiated from the specimen surface or near surface defects in the DSAWed samples and in the base metal as well.

4. Conclusions

1. The microstructure of the as-received AZ31B-H24 consisted of small elongated grains with some Mn–Al containing inclusions which were still present in different zones after welding. The FSW resulted in recrystallized and relatively small grains in the SZ and TMAZ, and partially recrystallized grains in the HAZ. After DSAW, fully recrystallized grains with a relatively large grain size were observed in the HAZ, and the divorced eutectic structure containing β-$Mg_{17}Al_{12}$ particles in the interdendritic and intergranular regions appeared in the fusion zone.
2. While the YS was higher, the UTS and ductility were lower in the FSWed samples than in the DSAWed samples. This was due to the premature fracture caused by the presence of welding defects in the FSWed samples at the bottom surface. The defects were also the cause for the small net flow stress from yielding up to the UTS in the FSWed samples. However, the strength of the FSWed samples was still similar to or higher than those reported in the literature due to the smaller grain sizes arising from the high speed low temperature FSW.
3. The strain-hardening capacity of the DSAWed samples was observed to be twice that of the base metal, with the strain-hardening capacity of FSWed samples lying in-between them. The strain-hardening exponents after both types of welding, evaluated via three different approaches, were all about two times higher than those of base metal.
4. A higher strain-hardening rate of the base metal at lower strains was observed due to smaller and pre-deformed grains where many dislocations had been generated in the base metal, coupled with stronger Hall–Petch contribution stemming from smaller grain sizes. At higher strains, the strain-hardening rate of the welded samples became higher due to the occurrence of recrystallization in the FSWed samples, and the larger grains together with β particles in the fusion zone in the DSAWed samples.
5. The YS, UTS, strain-hardening exponent and strain-hardening rate increased slightly, and ductility decreased with increasing strain rate. Stronger strain-rate sensitivity was observed in the base metal due to the smaller grain size and higher flow stress in comparison with the welded joints.

References

[1] X. Cao, M. Jahazi, Mater. Des. 30 (2009) 2033–2042.
[2] X.Z. Lin, D.L. Chen, J. Mater. Eng. Perform. 17 (2008) 894–901.
[3] A. Tharumarajah, P. Koltun, J. Clean. Prod. 15 (2007) 1007–1013.
[4] W.M. Thomas, E.D. Nicholas, J.C. Needham, M.G. Church, P. Templesmith, C.J. Dawes, GB Patent Application No. 9125978.9 (December 1991).
[5] N. Afrin, D.L. Chen, X. Cao, M. Jahazi, Mater. Sci. Eng. A 472 (2008) 179–186.
[6] H.W. Lee, T.S. Lui, L.H. Chen, J. Alloys Compd. 475 (2009) 139–144.
[7] H. Watanabe, H. Tsutsui, T. Mukai, K. Ishikawa, Y. Okanda, M. Kohzu, K. Higashi, Mater. Trans. A 42 (2001) 1200–1205.
[8] T. Mukai, M. Yamanoi, H. Watanabe, H. Higashi, Scripta Mater. 45 (2001) 89–94.
[9] A. Bussiba, A.B. Artzy, A. Shtechman, S. Ifergan, M. Kupiec, Mater. Sci. Eng. A 302 (2001) 56–62.
[10] ASM Metals Handbook 10th Edition, vol. 6, Welding, Brazing, and Soldering, 1990 ASM International, Materials Park, OH.
[11] Y.M. Zhang, S.B. Zhang, Method of arc welding using dual serial opposed torches, US Patent No. 5990446 (November 1999).
[12] Y.M. Zhang, C. Pan, A.T. Male, Metall. Mater. Trans. A 31 (2000) 2537–2543.
[13] Y.M. Zhang, C. Pan, A.T. Male, J. Mater. Sci. Lett. 19 (2000) 831–833.
[14] Y.M. Zhang, S.B. Zhang, Weld. J. 78 (1999) 202–206.
[15] Y.M. Zhang, S.B. Zhang, Weld. J. 77 (1998) 57–61.
[16] Y. Kwon, D.C. Weckman, Sci. Technol. Weld. Join. 13 (2008) 485–495.
[17] J.A. Moulton, D.C. Weckman, Weld. J. 89 (2010) 11s–23s.
[18] Y.J. Quan, Z.H. Chen, X.S. Gong, Z.H. Yu, Mater. Charact. 59 (2008) 1491–1497.
[19] L. Liu, C. Dong, Mater. Lett. 60 (2006) 2194–2197.
[20] J. Zhu, L. Li, Z. Liu, Appl. Surf. Sci. 247 (2005) 300–306.
[21] W. Woo, H. Choo, M.B. Prime, Z. Feng, B. Clausen, Acta Mater. 56 (2008) 1701–1711.
[22] X.H. Wang, K.S. Wang, Mater. Sci. Eng. A 431 (2006) 114–117.
[23] L. Commin, M. Dumont, J.-E. Masse, L. Barrallier, Acta Mater. 57 (2009) 326–334.
[24] N. Afrin, D.L. Chen, X. Cao, M. Jahazi, Scripta Mater. 57 (2007) 1004–1007.
[25] P.B. Srinivasan, R. Zettler, C. Blawert, W. Dietzel, Mater. Charact. 60 (2009) 389–396.
[26] L. Yu, K. Nakata, N. Yamamoto, J. Liao, Mater. Lett. 63 (2009) 870–872.
[27] R.S. Mishra, Z.Y. Ma, Mater. Sci. Eng. R 50 (2005) 1–78.
[28] R. Nandan, T. DebRoy, H.K.D.H. Bhadeshia, Prog. Mater. Sci. 53 (2008) 980–1023.
[29] S.H. Park, Y.S. Sato, H. Kokawa, Scripta Mater. 49 (2003) 161–166.
[30] H. Takuda, S. Kikuchi, N. Yoshida, H. Okahara, Mater. Trans. A 44 (2003) 2266–2270.
[31] L. Yu, K. Nakataa, J. Liao, J. Alloys Compd. 480 (2009) 340–346.
[32] W. Lee, K.-H. Chung, D. Kim, J. Kim, C. Kim, K. Okamoto, R.H. Wagoner, K. Chung, Int. J. Plast. 25 (2009) 1626–1654.
[33] U.F. Kocks, H. Mecking, Prog. Mater. Sci. 48 (2003) 171–273.
[34] J.A. del Valle, F. Carreno, O.A. Ruano, Acta Mater. 54 (2006) 4247–4259.
[35] J.A. del Valle, O.A. Ruano, Scripta Mater. 55 (2006) 775–778.
[36] J. Shen, G.Q. You, S.Y. Long, F.S. Pan, Mater. Charact. 59 (2008) 1059–1065.
[37] ASM Handbook, 10th Edition, vol. 2, Properties and Selection: Nonferrous Alloys and Special Purpose Materials, 1990, ASM International, Materials Park, OH.
[38] G.F. Vander Voort, Metallography Principles and Practice, ASM International, Materials Park, OH, USA, 1999.
[39] ASTM Standard E8/E8M, 2008, Standard Test Methods for Tension Testing of Metallic Materials, ASTM International, West Conshohohocken, PA, 2008.
[40] M. Fairman, N. Afrin, D.L. Chen, X.J. Cao, M. Jahazi, Can. Metall. Quart. 46 (2007) 425–432.
[41] W.B. Lee, Y.M. Yeon, S.K. Kim, Y.J. Kim, S.B. Jung, in: H.I. Kaplan (Ed.), Magnesium Technology 2002, TMS, 2002, pp. 309–312.
[42] J.A. Esparza, W.C. Davis, E.A. Trillo, L.E. Murr, J. Mater. Sci. Lett. 21 (2002) 917–920.
[43] M. Pareek, A. Polar, F. Rumiche, J.E. Indacochea, J. Mater. Eng. Perform. 16 (2007) 655–662.
[44] S. Lim, S. Kim, C.G. Lee, C.D. Yim, S.J. Kim, Metall. Mater. Trans. A 36 (2005) 1609–1612.
[45] X.Z. Lin, D.L. Chen, Mater. Sci. Eng. A 496 (2008) 106–113.
[46] L.M. Liu, G. Song, M.L. Zhu, Metall. Mater. Trans. A 39 (2008) 1702–1711.
[47] P. Liu, Y.J. Li, H.R. Geng, J.A. Wang, Mater. Lett. 61 (2007) 1288–1291.
[48] G. Ben-Hamu, D. Eliezer, C.E. Cross, Th. Böllinghaus, Mater. Sci. Eng. A 452–453 (2007) 210–218.
[49] S.F. Su, J.C. Huang, H.K. Lin, N.J. Ho, Metall. Mater. Trans. A 33 (2002) 1461–1473.
[50] G. Padmanaban, V. Balasubramanian, J.K. Sarin Sundar, JMPEG, in press.
[51] L. Jiang, J.J. Jonas, A.A. Luo, A.K. Sachdev, S. Godet, in: A.A. Luo, N.R. Neelameggham, R.S. Beals (Eds.), Magnesium Technology, TMS, 2006, pp. 233–238.
[52] Y.M. Wang, E. Ma, Mater. Sci. Eng. A 375–377 (2004) 46–52.
[53] V. Livescu, C.M. Cady, E.K. Cerreta, B.L. Henrie, G.T. Gray II, in: A.A. Luo, N.R. Neelameggham, R.S. Beals (Eds.), Magnesium Technology, TMS, 2006, pp. 153–158.
[54] K. Elangovan, V. Balasubramanian, M. Valliappan, Int. J. Adv. Manuf. Technol. 38 (2008) 285–295.
[55] R.W. Davies, M.T. Smith, H.E. Oliver, M.A. Khaleel, S.G. Pitman, Metall. Mater. Trans. A 31 (2000) 2755–2763.
[56] C.J. Bayley, A.K. Pilkey, Mater. Sci. Eng. A 403 (2005) 1–10.
[57] J. Luo, Z. Mei, W. Tian, Z. Wang, Mater. Sci. Eng. A 441 (2006) 282–290.
[58] W.D. Callister Jr., Materials Science and Engineering – An Introduction, 8th Edition, John Wiley & Sons, Inc., New York, USA, 2009.
[59] G.E. Dieter, Mechanical Metallurgy, 3rd Edition, McGraw-Hill, MA, USA, 1986.
[60] W.F. Hosford, Mechanical Behavior of Materials, Cambridge University Press, New York, USA, 2005.
[61] J. Yang, B.L. Xiao, D. Wang, Z.Y. Ma, Mater. Sci. Eng. A 527 (2010) 708–714.
[62] J.H. Hollomon, Trans. AIME 162 (1945) 268–289.
[63] R.W. Hertzberg, Deformation and Fracture Mechanics of Engineering Materials, 4th Edition, John Wiley & Sons, New York, USA, 1996.
[64] L. Ratke, P.I. Welch, 13th Biennial Congress – International Deep Drawing Research Group: Efficiency in Sheet Metal Forming, Melbourne, Australia, 1984, pp. 427–435.
[65] X.H. Chen, L. Lu, Scripta Mater. 57 (2007) 133–136.
[66] P. Ludwik, Elemente der Technologischen Mechanik, Springer-Verlag OHG, Berlin, 1909, p. 32.
[67] M. Srinivasan, T.G. Stoebe, J. Mater. Sci. 9 (1974) 121–128.
[68] A.D. Rollett, U.F. Kocks, Sol. Stat. Phenom. 35–36 (1994) 1–18.
[69] W. Pantleon, Mater. Sci. Eng. A 387–389 (2004) 257–261.
[70] C.W. Sinclair, W.J. Poole, Y. Brechet, Scripta Mater. 55 (2006) 739–742.
[71] I. Kovacs, N.Q. Chinh, E. Kovacs-Csetenyi, Phys. Status Solidi A 194 (2002) 3–18.
[72] J.A. del Valle, A.C. Picasso, R. Romero, Acta Mater. 51 (2003) 6443–6452.
[73] M.R. Barnett, Z. Keshavarz, A.G. Beer, D. Atwell, Acta Mater. 52 (2004) 5093–5103.
[74] U.S. Lindholm, J. Mech. Phys. Solids 12 (1964) 317–335.
[75] Y.V.R.K. Prasad, R.W. Armstrong, Philos. Mag. 29 (1974) 1421–1425.